Chemical Physics Letters 787 (2022) 139282

Contents lists available at ScienceDirect

Chemical Physics Letters

journal homepage: www.elsevier.com/locate/cplett

Analysis of spectator chemical bonds in S_N2@C and @Si reaction mechanisms in the gas phase

Carlos V. Santos-Jr [a], Miguel A. F. de Souza [a], Elfi Kraka [b], Renaldo T. Moura Jr [c,*]

[a] Institute of Chemistry, Federal University of Rio Grande do Norte, Natal, RN, Brazil
[b] Department of Chemistry, Southern Methodist University, Dallas, TX
[c] Department of Chemistry and Physics, Center of Agrarian Sciences, Federal University of Paraíba, Areia, PB, Brazil

ARTICLE INFO

Keywords:
QTAIM
Overlap model
Local Vibrational Modes
S_N2 reactions

ABSTRACT

In this work, Cl^-+AR_3Cl reactions (with A = C and Si, and R = H, Me, Et, Cl, and F) were investigated to evaluate the A–R spectator bond properties at the ω-B97X-D/SPK-TZP level of theory, applying the Quantum Theory of Atoms in Molecules, the Overlap Model, and Local Vibrational Mode theory. The different chemical bond analyses converge to the conclusion (in line with current literature) that the steric hindrance experienced by Cl^- in S_N2@C reactions can be viewed as a consequence of the greater covalent nature of C—R bonds that concentrate density in bond region more efficiently than Si—R.

1. Introduction

Understanding the key aspects of chemical reaction mechanisms is usually focused on the characterization of the potential energy surface (PES) [1–3] targeting in particular structural and energetic properties of the stationary points, i.e., reactants, products, intermediates, and transition states (TS). A more complete picture can be obtained by following the reaction complex (unity of reacting species) along the reaction path from entrance to exit channel, as realized in the unified reaction valley approach which correlates all chemical events including bond breaking/formation to the curvature of the reaction path [4]. Recent studies have suggested that chemical bond analysis methods can provide details about the evolution of bonding during a chemical reaction [5–10] when applied to points along the energy profile. E.g., (i) Farfán et al. [6,7] investigated the stereoselectivity of Witting reactions applying different bond analysis methodologies. They concluded that the degree of advancement of the emerging C—C bond is intimately tied to the stereochemistry of the reaction product. (ii) Oliveira et al. [8] used a wide variety of chemical bond descriptors for a series of fluorination reactions to study the nature of X—F bonds (with X = B, C, N, O, and F) and also to understand the covalent, hypervalent, and noncovalent bonds in these compounds. [8]

An attractive target reaction for the exploration of different bond analysis methods is the bimolecular nucleophilic substitution (S_N2) [11–16]. Classically, the mechanism of the S_N2 reaction is described by a single kinetic step that comprises the attack of a nucleophile (Nu^-) at the backside, opposite to the leaving group (X) of the AR_3X reagent to yield the $NuAR_3$ product with configuration inversion. As shown in Fig. 1, a $[Nu\cdots AR_3\cdots X]^-$ pentacoordinate intermediate separates the reactants and products. In the $[Nu\cdots AR_3\cdots X]^-$ intermediate, the substituent groups (R) are forced into a planar trigonal rearrangement as a consequence of the repulsive action around the central atom (A).

Bickelhalput et al. [17,18] investigated a series of S_N2@A (A = C, Si, and P) reactions in the gas phase following the scheme depicted in Fig. 1. Fig. 2 shows four possible energy profiles for these type of reactions.

(a) ***Single-peak profile***, where the TS represents the high point of the potential energy surface;
(b) ***Single-well profile***, where a single stable transitional complex (TC) is formed;
(c) **Double-well profile**, with two stable ion–dipole complexes between the TS and the reagents/products, here labeled as reactant complex (RC) and product complex (PC);
(d) ***Triple-well profile***, where three minimum stationary points (RC, PC, and TC) and two maximum (pre-TS and post-TS, being before and after the TC, respectively) are obtained.

A well-marked feature of the profiles depicted in Fig. 2 consists of the nature of the pentacoordinate intermediate. For the S_N2@C reactions in black or blue colour, the $[Nu\cdots CR_3\cdots X]^-$ structure corresponds to a

* Corresponding author.
E-mail address: renaldo.mourajr@cca.ufpb.br (R.T. Moura Jr).

https://doi.org/10.1016/j.cplett.2021.139282
Received 26 November 2021; Accepted 6 December 2021
Available online 7 December 2021

saddle point (=TS) on the potential energy surface. For the S_N2@Si reactions in red color the $[Nu\cdots SiR_3\cdots X]^-$ species often forms a stable intermediate (=TC).

Interestingly, in S_N2@P reactions (particularly for $Nu^- + POR_2X$) all four types of profiles can be obtained depending on the nature of Nu^-, X, and R [16]. The energy decomposition analysis (EDA) has revealed that an interplay between the steric (Pauli) repulsion and the electronic effects can explain the distinct shapes of the PES in the gas phase S_N2@A reactions [17–19]. Recently the quantum theory of atoms in molecules (QTAIM) [20] and natural bond orbital (NBO) [21] analysis have shown that hydrogen and σ-hole bonding can be responsible for the formation of triple-well profile in some S_N2@Si reactions [9]. Alkorta and Elguero [22] studied S_N2@C, @N, @Si, and @P reactions and pointed to the existence of valence expansion effect in the S_N2@P reaction.

Thomas et al. [23] studied the rate of an S_N2@Si reaction with a fluoride nucleophile. The reaction rate decreased by a factor of up to 5.5 by coupling the Si—C vibrational stretching modes (Si – leaving group bonding) to the zero-point fluctuations of a resonant infrared microfluidic cavity [23]. Climent and Feist [24] reported the experimental modification of the chemical reactivity of S_N2@Si reactions under vibrational strong coupling (VSC) in microfluid cavities. They showed that certain modes of their studied S_N2@Si reactions are highly coupled among the different fragments and that it is difficult to find normal isolated stretching modes to elucidate VSC experiments. Hansen et al. [25] applied the Activation Strain Model [26] extended with EDA [27] to study the enhanced reactivity of α-nucleophiles and concluded that orbital overlap between the HOMO lobe on the α-nucleophile and the substrate influences Nu ⋯ substrate Pauli repulsion.

Chemical bond analyses generally target $[Nu \cdots AR_3X]^-$ or $[NuAR_3 \cdots X]^-$ interactions missing out the analysis of spectator bonds A—R bonds. Therefore, to advance our understanding of the S_N2 mechanism in the gas phase, we investigated in this work the stationary points of the $Cl^- + AR_3Cl$ reactions (with A = C and Si, and R = H, Me, Et, Cl, and F) with chemical bond analyses applied to the A—R bonds. An important aspect of this study was to evaluate the nature of A—R bonding in particular at the TS and TC pentacoordinate structures. Quantum Theory of Atoms in Molecules (QTAIM) [20], Overlap Model (OP) [28], and Local Vibrational Mode (LVM) theory [29] were used to further study the A—R bond interaction along the S_N2@C and S_N2@Si profiles at different stages of the S_N2@A reactions.

2. Methodology

The three bond analysis methods are briefly described in the following subsections.

2.1. The chemical bond overlap model

OP was recently introduced [28,30] and is implemented in our ChemBOS code. OP can be successfully applied to analyze chemical bonds in compounds of different complexity, e.g., simple diatomic molecules, coordination compounds, and solid-state systems [30–33]. It is possible to interpret 4*f*-4*f* transitions intensities in terms of covalency [32,34]. Details can be found in [28].

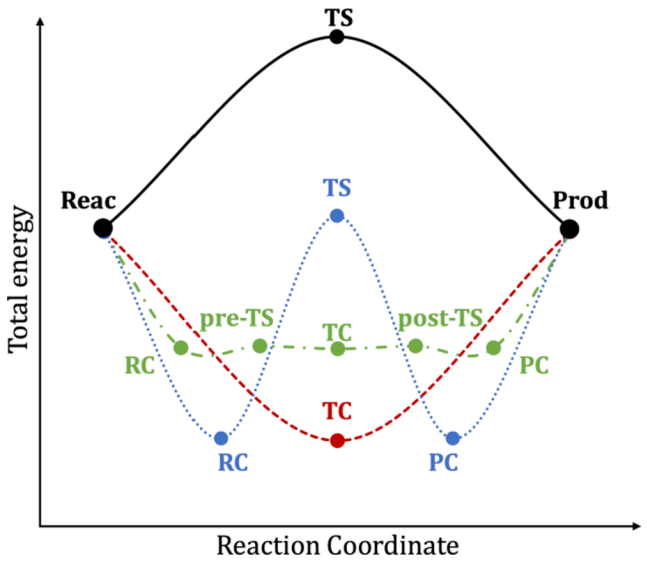

Fig. 2. Typical profiles for thermoneutral S_N2 reactions in gas phase: single-peak (solid black line), single-well (dash red line), double-well (dot blue line), and triple-well (dash and dot green line). Reac = reactant, RC = reactant complex, TC = transitional complex, TS = transition state, PC = product complex, and Prod = product.

Given a localized molecular orbital (LMO) *l*, attributed to a chemical bond A—B in a molecular system, overlap population density maps can be generated from

$$\rho^l_{OP}(\vec{r}) = 2\sum_{i\in A}^{m}\sum_{j\in B}^{m} c_{li}c_{lj}\varphi_{li}(\vec{r})\varphi_{lj}(\vec{r}) \quad (1)$$

where *m* is the number of atomic orbitals or basis functions, $\varphi_{li}(\vec{r})$ are the primitive or contracted functions, and c_{li} are the coefficients of the LMOs.

The overlap population p^l is then obtained from the integration of Eq. (1) for a N_{occ} LMO occupation number,

$$p^l = N_{occ} \bullet 2\sum_{i\in A}\sum_{j\in B} c_{li}c_{lj}S^l_{ij} \quad (2)$$

where S^l_{ij} are the overlap integrals.

The anisotropic overlap polarizability $\overline{\alpha}_{OP}$ can be calculated from the tensor

$$\overline{\alpha}_{OP} = \frac{1}{3}\left(\alpha^{xx}_{OP} + \alpha^{yy}_{OP} + \alpha^{zz}_{OP}\right) \quad (3)$$

where each term is calculated by

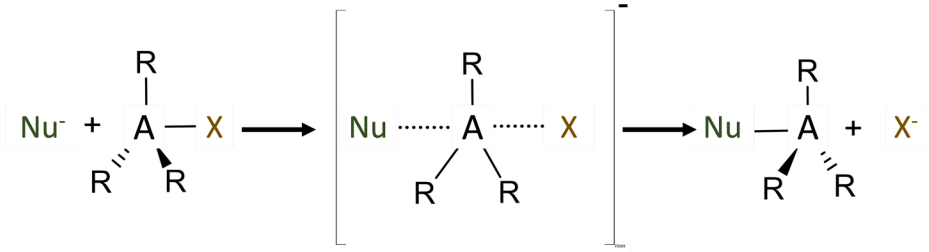

Fig. 1. Walden inversion mechanism of the S_N2 reaction. R = substituent groups; Nu^- = nucleophile, X = leaving group, and A = central atom.

$$\alpha_{OP}^{\kappa\lambda} = -\frac{2}{F_\kappa}\left(\sum_{\substack{i\in A\\ i\in B}}^{m}\sum_{\substack{j\in B\\ j\in A}}^{n} c_i^{'}c_j^{'}\langle\varphi_i|\lambda|\varphi_j\rangle - \sum_{\substack{i\in A\\ i\in B}}^{m}\sum_{\substack{j\in B\\ j\in A}}^{n} c_i^{0}c_j^{0}\langle\varphi_i|\lambda|\varphi_j\rangle\right) \quad (4)$$

where c_i^0 and $c_i^{'}$ are the expansion coefficients for the unperturbed and perturbed LMO, that can be obtained by a self-consistent field (SCF) procedure followed by a localization unitary transformation. In Eq. (4), κ is the direction in which the electrical field F_κ is applied, and can be equals to x, y or z. Similarly, λ (than can be x, y or z) defines the direction in which the dipole (induced by F_κ) will be inspected.

The so-called intra-overlap Coulomb repulsion, that occurs within the overlap of the chemical bond described by the LMO l, is defined as

$$J_{OP}^{l,l} = \int \rho_{OP}^{l}(\vec{r}_1) r_{12}^{-1} \rho_{OP}^{l}(\vec{r}_2) d\vec{r}_1 d\vec{r}_2 \quad (5)$$

where ρ_{OP}^{l} is described by Eq. (1). $J_{OP}^{l,l}$, from here denoted by J_{OP}^{intra} is a 6D integration, that is solved numerically [35].

2.2. The local vibrational modes theory

LVM, originally introduced by Konkoli and Cremer [29,36], provides through its local stretching force constant, a unique measure of the intrinsic strength of a chemical bond [37]. The local mode force constant, for a local mode n, is obtained via Eq. (6) [29]:

$$k_n^a = \left(d_n K^{-1} d_n^{+}\right)^{-1} \quad (6)$$

where d_n is the n th normal mode in internal coordinates and diagonal matrix K is the force constant in normal mode coordinates. Both quantities can be obtained via a standard normal mode analysis, available in most of the common quantum chemistry packages [29].

2.3. The quantum theory of atoms in molecules

QTAIM was used in this work to assess the covalent character of the A—R bonds applying the Cremer-Kraka criterion [38], which is based on the local energy density $H(r_{BCP})$ evaluated at the bond critical point BCP

$$H(r_{BCP}) = G(r_{BCP}) + V(r_{BCP}) \quad (7)$$

where $G(r_{BCP})$ is the kinetic energy and $V(r_{BCP})$ is the potential energy, both calculated at the BCP position r_{BCP}. Given that $G(r_{BCP})$ is destabilizing (and positive) and $V(r_{BCP})$ is stabilizing (and negative), the Cremer-Kraka criterion states that $H(r_{BCP}) < 0$ indicates a covalent interaction, while $H(r_{BCP}) > 0$ indicates an electrostatic interaction. We also used the Laplacian $\nabla^2\rho(r_{BCP})$, that holds information about local charge concentration ($\nabla^2\rho(r_{BCP}) < 0$) or depletion ($\nabla^2\rho(r_{BCP}) > 0$) [20].

3. Computational procedure

Geometry optimization and frequency calculations were performed with the ω-B97X-D [39] functional, and SPK-TZP basis set [40] using GAMESS [41] and Gaussian16 [42]. The QTAIM, OP, and LVM descriptors were calculated with the Multiwfn [43], ChemBOS [35], and LmodeA [44] software, respectively. For the overlap properties, the Pipek-Mezey molecular orbital localization [45] was applied.

4. Results and discussion

The energy profiles for the reactions studied in this work leading to 44 stationary points are summarized in Fig. 3 (10 reacts, 10 prods, 5 RCs, 5 PCs, 2 pre-TSs, 2 post-TSs, 5 TSs, and 5 TCs); energies are given relative to reactants. For the S_N2@C reactions, reactants and products are separated by a pentacoordinate transition state (TS), corresponding to a saddle point on the PES, with a single-peak profile for R═F and Cl, and a double-well profile for R═H, Me, and Et. In contrast, for S_N2@Si reactions, a stable pentacoordinate transition complex (TC) is observed for all structures with R═H, Me, Et, F, and Cl, with a single-well profile for R═H, F, and Cl, and a triple-well for R═Me and Et with a pre-TS and a post-TS in each case.

These findings are in line with earlier work [12], as well as the relative energies shown in Fig. 3 [22]. The stabilization in the double-well and triple-well profiles seems to be a consequence of an ion–dipole interaction. The TS/TC formation found in this work can be associated with steric effects matching the findings of Bento and Mathias [12].

All stationary points were characterized as local energy minima (Reac, Prod, RC, PC, and TC) or transition states of first order (pre-TS, TS, and post-TS) with the normal mode of the imaginary harmonic frequency being associated with the nucleophilic attack path. The A—R bonds in Reacs, TCs, and TSs were analyzed using the three bond analyses described above. The results are summarized in Table 1, depicting overlap properties, QTAIM descriptors and local modes force constants.

In the following main bond property trends of the A—R spectator bonds are discussed focusing on two major aspects: i) how does each analysis methodology characterize bonding in C—R and Si—R bonds, and ii) what is the relationship between the three analysis methods applied in this work.

Fig. 4 visualizes the main results shown in Table 1. The general trend

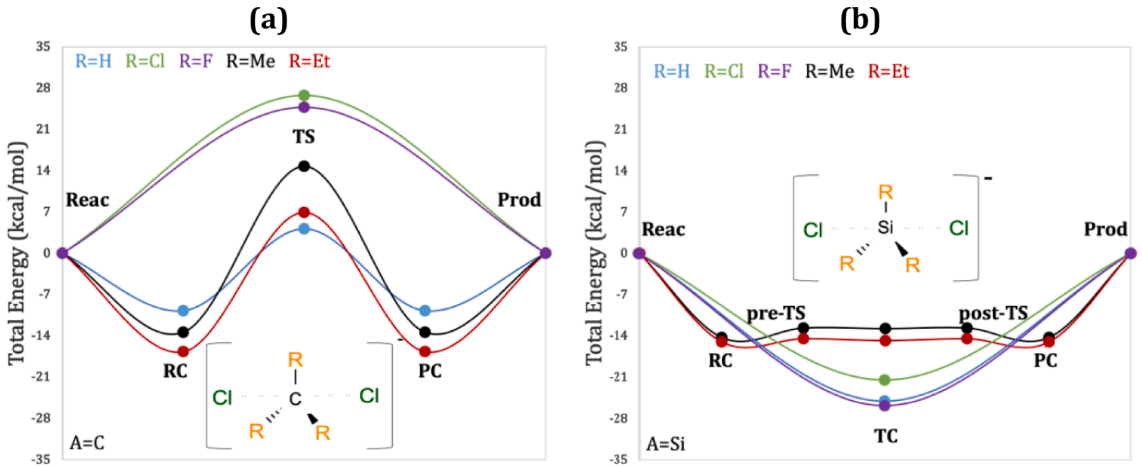

Fig. 3. Energy profiles obtained for the Cl^- + AR_3Cl S_N2 reactions, where A = C, Si, and R = H, F, Cl, Me, and Et. Reac = reactants, RC = reactant complex, pre-TS = pre transition state, TS = transition state, post-TS = post transition state; TC = transition complex, PC = product complex, and Prod = products.

Table 1
Spectator bonds (A—R) properties obtained for the Reac, TC, and TS structures: bond distance D (in Å); overlap density ρ_{OP} (in e), polarizability α_{OP} (in Å^3), and repulsion J_{OP}^{intra} (in E_h); density ρ_{BCP} (in e/a_0^3), Laplacian of the density $\nabla^2\rho_{BCP}$ (in e/a_0^5), and local energy density H_{BCP} (in E_h/a_0^3) at the critical point; local mode force constant k_n^a (in mDyn/Å).

					Overlap properties			QTAIM			LVM
Entry		**System**	**Bond**	**D**	ρ_{OP}	α_{OP}	J_{OP}^{intra}	ρ_{BCP}	$\nabla^2\rho_{BCP}$	H_{BCP}	k_n^a
1	Reactant	CH_3Cl	C–H	1.091	0.890	0.177	0.570	0.292	−1.184	−0.340	5.218
2		CMe_3Cl	C–C	1.530	0.815	0.465	0.505	0.249	−0.625	−0.216	3.708
3		CEt_3Cl	C–C	1.541	0.817	0.352	0.505	0.239	−0.568	−0.197	3.284
4		CF_3Cl	C–F	1.338	0.647	0.070	0.415	0.296	−0.562	−0.461	5.022
5		CCl_3Cl	C–Cl	1.782	0.713	0.311	0.376	0.196	−0.255	−0.130	2.179
6	Transition state	Cl ··· CH_3 ··· Cl	C–H	1.075	0.924	0.263	0.607	0.307	−1.381	−0.380	5.845
7		Cl ··· CMe_3 ··· Cl	C–C	1.490	0.795	0.468	0.507	0.250	−0.637	−0.217	3.885
8		Cl ··· CEt_3 ··· Cl	C–C	1.492	0.826	0.491	0.536	0.245	−0.604	−0.208	3.790
9		Cl ··· CF_3 ··· Cl	C–F	1.290	0.664	0.169	0.459	0.351	−0.524	−0.614	6.240
10		Cl ··· CCl_3 ··· Cl	C–Cl	1.688	0.741	0.395	0.417	0.256	−0.543	−0.222	3.341
11	Reactant	SiH_3Cl	Si–H	1.487	0.851	0.624	0.438	0.125	0.106	−0.086	2.779
12		$SiMe_3Cl$	Si–C	1.881	0.854	0.344	0.475	0.124	0.147	−0.081	2.232
13		$SiEt_3Cl$	Si–C	1.898	0.879	0.330	0.488	0.122	0.115	−0.081	2.459
14		SiF_3Cl	Si–F	1.583	0.592	0.498	0.365	0.147	1.085	−0.046	5.507
15		$SiCl_3Cl$	Si–Cl	2.040	0.682	0.427	0.312	0.107	0.213	−0.062	2.782
16	Transition complex	Cl ··· SiH_3 ··· Cl	Si–H	1.484	0.882	0.533	0.460	0.125	0.114	−0.086	2.713
17		Cl ··· $SiMe_3$ ··· Cl	Si–C	1.903	0.908	0.604	0.511	0.124	0.119	−0.081	2.585
18		Cl ··· $SiEt_3$ ··· Cl	Si–C	1.921	0.904	0.567	0.504	0.119	0.066	−0.082	2.309
19		Cl ··· SiF_3 ··· Cl	Si–F	1.621	0.584	0.190	0.329	0.142	1.021	−0.040	4.129
20		Cl ··· $SiCl_3$ ··· Cl	Si–Cl	2.128	0.637	0.228	0.260	0.098	0.158	−0.055	1.649

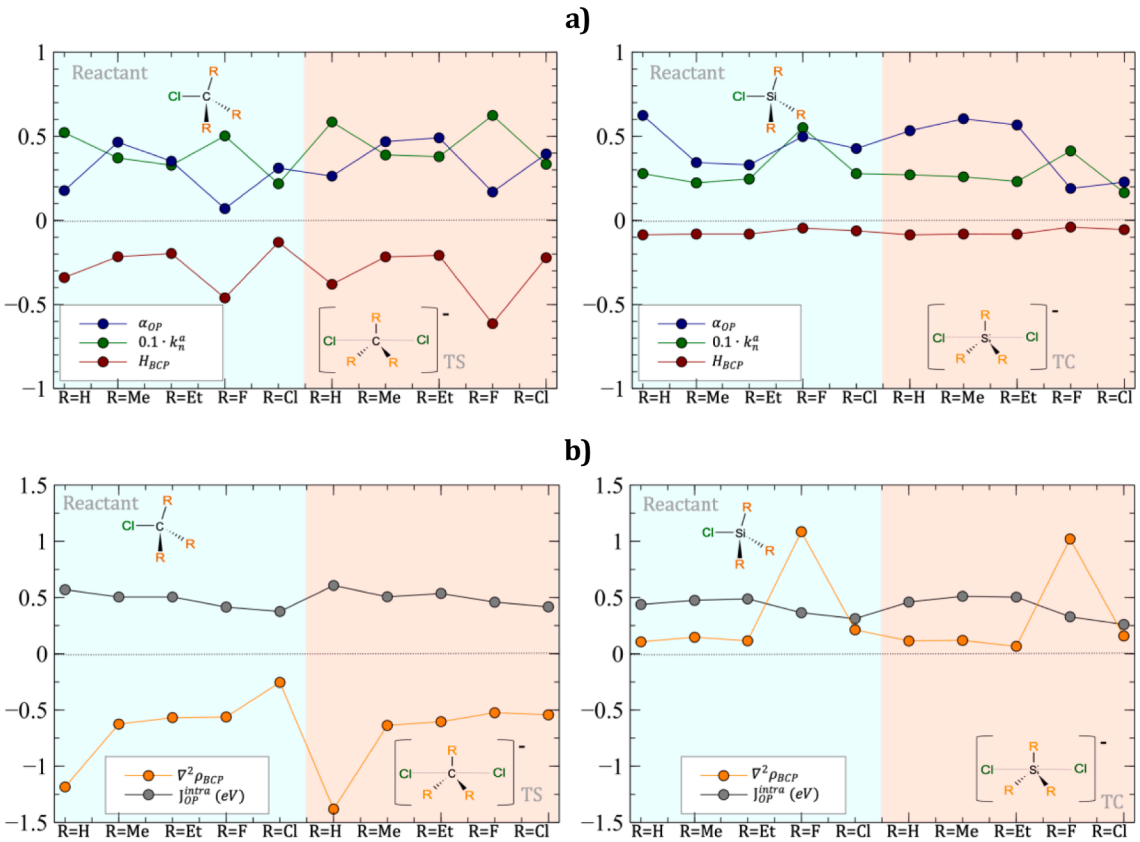

Fig. 4. Graphical representation of the spectator bonds (A–R) properties for the Reac (left side, light blue background), TC/TS (right side, light red background) structures: a) overlap polarizability α_{OP} (in Å^3), local energy density H_{BCP} (in E_h/a_0^3) at the critical point, and repulsion J_{OP}^{intra} (in E_h); density ρ_{BCP} (in e/a_0^3), Laplacian of the density $\nabla^2\rho_{BCP}$ (in e/a_0^5), and; local mode force constant k_n^a (in mDyn/Å) – scaled by 0.1 for visualization purposes.

for the C—R bonds is an increase of H_{BCP}, i.e., reduced covalent character is in line with a decrease in the local force constant k_n^a, which indicates a decrease in the bond strength. An increase of α_{OP} indicates that the overlap density is being more polarizable. For Si—R bonds, the H_{BCP} values are smaller than those of the C—R and closer to 0.0 E_h/a_0^3, reflecting the well-known fact that Si—R bonds are generally less covalent than the C—R bonds [46]. Variations in α_{OP} and k_n^a show a parallel trend for Si—R bonds of the reactants, and an opposite trend for the TC structures.

Fig. 4b depicts the $\nabla^2\rho_{BCP}$ and J_{OP}^{intra} properties for the studied bonds. C—R bonds exhibit an inverse relationship between $\nabla^2\rho_{BCP}$ and J_{OP}^{intra}. This is expected, given that a less negative $\nabla^2\rho_{BCP}$ indicates a charge depletion at the critical point, and that chemical bonds with a charge depletion tend to have smaller J_{OP}^{intra} (less overlap density intra-repulsion) values [28].

Fig. 5 visualizes the relationship between H_{BCP} and $\nabla^2\rho_{BCP}$. All C—R chemical bonds (empty and filled circles in Fig. 5) have negative $\nabla^2\rho_{BCP}$ values while the Si—R values are positive. The H_{BCP} for Si—R bonds are in range –0.1 $E_h/a_0^3 < H_{BCP} <$ 0.0 E_h/a_0^3, while for C—R bonds are in range –0.7 $E_h/a_0^3 < H_{BCP} <$ –0.1 E_h/a_0^3 again reflecting the fact that C—R bonds are generally more covalent than their higher homologues, concentrating more electron density in the interatomic region. There is no significant difference between Si—R bonds of reactants and TS-TC, whereas QTAIM indicates that C—R bonds are generally more covalent in the TS/TC than in the Reac structure (filled circles with more negative H_{BCP} and $\nabla^2\rho_{BCP}$ values than empty circles). C—F bonds in reactant and TS are the exceptions in which the more covalent bond (smaller H_{BCP}) does not exhibit more density concentration in the bond region (smaller $\nabla^2\rho_{BCP}$), see Fig. 5, when compared with C—C bonds in reactants.

Recently, Blokke and coworkers [47] applied the Activation Strain Model [26] extended with EDA [27] to study archetypal $H_3C—CH_3$, $H_3C—F$, and $H_3C—Cl$ molecules, among others, revealing that from C—F to C—Cl the expected bond weakening effect is caused primary by Pauli repulsion, not because of decreasing electronegativity difference. These authors pointed to the increase in effective atomic size from F to Cl and its more extended atomic orbitals which lead to an increase in occupied molecular orbitals overlap (S) [47]. Similarly, the results reported in the present work corroborate these trends. In C—F bonds (Entries 4, and 9 in Table 1), despite having smaller equilibrium bond distances than C—Cl bonds (Entries 5, and 10 in Table 1), the ρ_{OP} values are smaller. A more diffuse valence shell interaction causes the overlap polarizability α_{OP} values for the C—Cl bonds to be greater than that of the C—F counterparts. As a consequence, despite being more covalent (smaller H_{BCP}), C—F bonds exhibit a bond charge concentration ($\nabla^2\rho_{BCP}$) similar to C—C bonds, and smaller overlap density ρ_{OP} and polarizability α_{OP}.

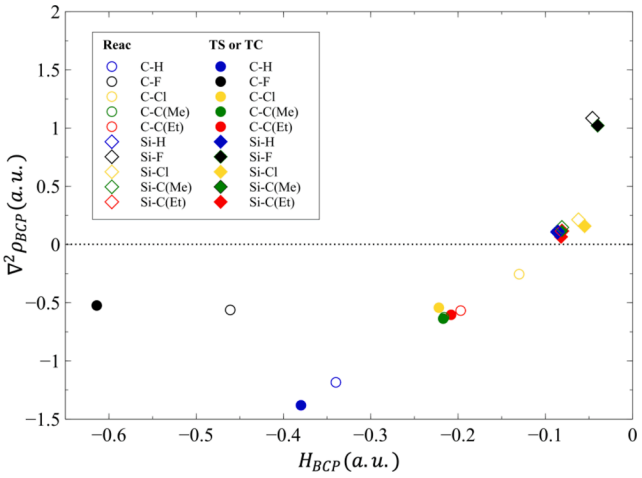

Fig. 5. QTAIM descriptors $\nabla^2\rho_{BCP}$ (in e/a_0^5), and H_{BCP} (in E_h/a_0^3) of the spectator chemical bonds A–R in reactants AR_3Cl and TS/TC Cl ⋯ AR_3 ⋯ Cl, (X = C, Si).

The overlap polarizability α_{OP} concept introduced by Malta and coworkers in 2002 [30] revealed an approximated analytical expression for α_{OP}, in a relationship with overlap integral ρ, bond distance R, and HOMO-LUMO gap $\Delta\varepsilon$ quantities of type: $\alpha_{OP}\ R^2\rho^2/\Delta\varepsilon$. Interestingly, Blokker and coworkers [47] pointed to a relationship between the orbital interaction ΔE_{oi} (that accounts for electron-pair interaction, charge transfer, and polarization), and the orbital overlap S (direct), and the orbital–orbital energy gap (inverse).

EDA [17–19] has revealed that the steric (Pauli) repulsion and electronic effects can explain the distinct shapes of the PES in the gas phase S_N2@A reactions. Our results support these findings, given that the steric hindrance experienced by Cl^- in S_N2@C reactions can be viewed as a consequence of the greater covalent nature of C—R bonds, that concentrates density along the chemical bond more efficiently than in Si—R. Also, C—R bonds are generally shorter than Si—R bonds, therefore the CR_3 core is more compact than the SiR_3 core.

Distance D and k_n^a values for the C—R and Si—R bonds in reactants and TS (see Table 1, entries 1–10, and Fig. 6a) are qualitatively connected via a generalized Badger type [48] relationship. It is noteworthy that the shorter bond is not always the stronger bond, as documented in literature [48–51]. As expected, C—R bonds investigated in this work are stronger (larger k_n^a values) than their Si—R counterparts, see Fig. 6b. Also, the k_n^a values for C—R bonds are larger in reactants than in TS/TC stationary points. The results found in this work corroborate the literature [47] values of bond dissociation energies (BDE) increasing from $H_3C—CH_3$ to $H_3C—F$ and decreasing from $H_3C—F$ to $H_3C—Cl$.Fig. 6.

Following this trend, the overlap properties point to C—R bonds with greater density concentration than for Si—R bonds, as represented in overlap density maps in Fig. 7. Also, the overlap Coulomb repulsion energy (J_{OP}^{intra}) is generally greater in C—R than in Si—R in AR_3Cl reactant systems, as can be seen in Table 1 and Fig. 4. As can be seen in Fig. 7, the overlap density maps of C—R bonds in both Reac and TS show a density concentration when compared with Si—R bonds.

It has to be pointed out that the overlap density maps must be analysed together with the overlap properties shown in Table 1; e.g., A—F bonds appear to have a large overlap density concentration, but if the corresponding ρ_{OP} and J_{OP}^{intra} values (entries 4, 9, 14, and 19 in Table 1) are taken into consideration, one sees that the overlap density and intra-repulsion are smaller than for other bonds.

5. Conclusions

Cl^- + AR_3Cl reactions (where A=C and Si, and R=H, Me, Et, Cl, and F) were investigated and A—R chemical bond properties were calculated using QTAIM, OP, and LVM. The different chemical bond analysis tools used in this work converge to the conclusion (in line with current literature) that the steric hindrance experienced by Cl^- in S_N2@C reactions can be viewed as a consequence of the greater covalent nature of C—R bonds, that concentrate density along the chemical bond more efficiently than in Si—R. In summary, H_{BCP} values for C—R bonds are more negative than for Si—R bonds. $\nabla^2\rho_{BCP}$ are negative for C—R bonds and positive for Si—R bonds. The C—F bonds in reactant and TS were found to be exception cases in H_{BCP} vs. $\nabla^2\rho_{BCP}$ observed trend, what is connected with the smaller ρ_{OP} and α_{OP} (compared to C—Cl counterpart) values. The local vibrational analysis reveals that distance D and k_n^a values for the studied bonds in reactants and TS/TC stationary points are qualitatively connected via a generalized Badger type relationship. The OP model points to a more efficient overlap density concentration in C—R bonds, when compared with Si—R ones, also supporting the QTAIM and LVM indicatives.

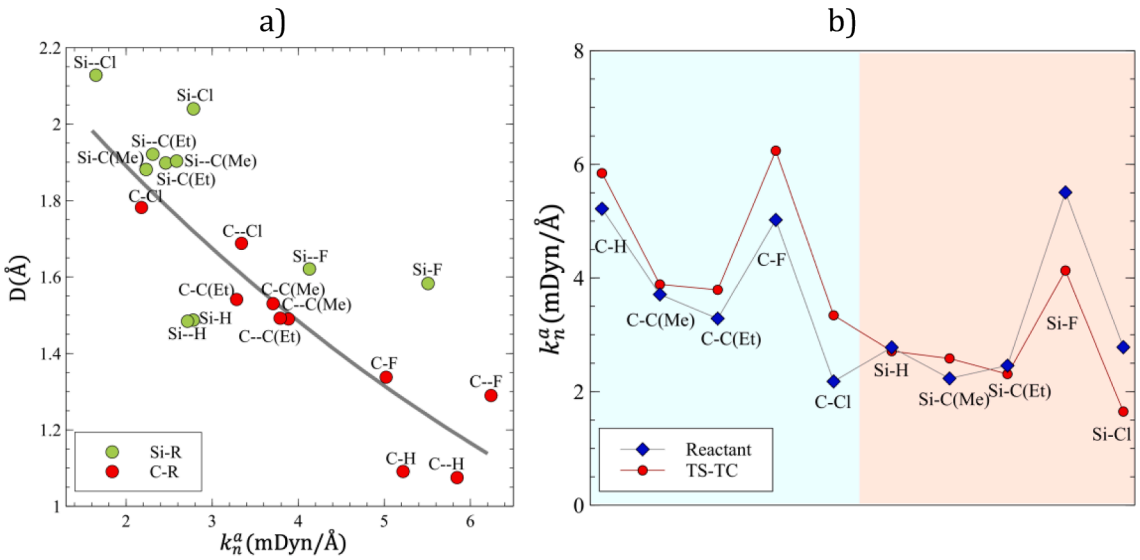

Fig. 6. (a) A–R distance D vs. Local stretching force constant k_n^a (in mDyn/Å), and (b) k_n^a()A–R) for reactants and TS/TC structures.

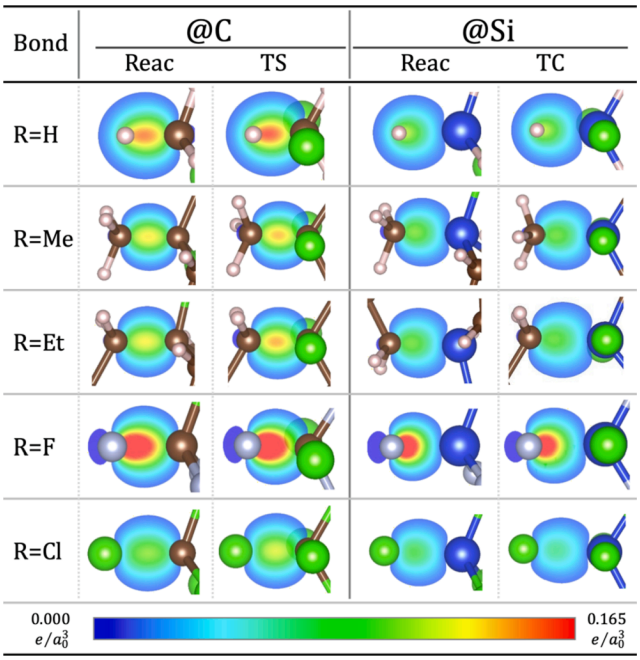

Fig. 7. Overlap density maps for C—H and Si—H bonds in CH_3Cl and SiH_3Cl structures.

CRediT authorship contribution statement

Carlos V. Santos-Jr: Software, Methodology, Formal analysis, Investigation, Writing – original draft. **Miguel A. F. de Souza:** Methodology, Writing – original draft, Supervision. **Elfi Kraka:** Methodology, Writing – original draft, Writing – review & editing, Funding acquisition. **Renaldo T. Moura Jr:** Conceptualization, Software, Methodology, Formal analysis, Investigation, Writing – original draft, Writing – review & editing.

Declaration of Competing Interest

The authors declare that they have no known competing financial interests or personal relationships that could have appeared to influence the work reported in this paper.

Acknowledgments

The Brazilian authors are grateful for the financial support from CNPq and CAPES agencies. This work was funded by the Brazilian Public Call n. 03 Produtividade em Pesquisa PROPESQ/PRPG/UFPB project number PVN13305-2020, PROPESQ/CNPq/UFPB PIN11132-2019 and CAPES No. 88882375143/2019-01. This research was funded by the National Science Foundation Grant No. CHE-1464906. The authors thank SMU and NPAD/UFRN for generously providing computational resources.

References

[1] T. Kudo, T. Higashide, S. Ikedate, H. Yamataka, Reaction profiles and substituent effects for the reduction of carbonyl compounds with monomer and dimer simple metal hydride reagents, J. Org. Chem. 70 (13) (2005) 5157–5163, https://doi.org/10.1021/jo050435a.
[2] P.R. Rablen, B.D. Mclarney, B.J. Karlow, J.E. Schneider, How Alkyl Halide Structure A ff ects E2 and S, J. Org. Chem. 867–879 (2014).
[3] M.M. Quintano, G.L.S. Rodrigues, M.A. Chagas, W.R. Rocha, Revisiting the tropospheric oh-initiated unimolecular decomposition of chlorpyrifos and chlorpyrifos-methyl: A theoretical perspective, J. Phys. Chem. A. 124 (21) (2020) 4280–4289, https://doi.org/10.1021/acs.jpca.0c02006.
[4] E. Kraka, W. Zou, Y. Tao, M. Freindorf, Exploring the mechanism of catalysis with the unified reaction valley approach (URVA)—A review, Catalysts 10 (2020) 691, https://doi.org/10.3390/catal10060691.
[5] S. Nanayakkara, E. Kraka, A new way of studying chemical reactions: A hand-in-hand URVA and QTAIM approach, Phys. Chem. Chem. Phys. 21 (27) (2019) 15007–15018.
[6] P. Farfán, S. Gómez, A. Restrepo, Dissection of the mechanism of the wittig reaction, J. Org. Chem. 84 (22) (2019) 14644–14658, https://doi.org/10.1021/acs.joc.9b02224.
[7] P. Farfán, S. Gómez, A. Restrepo, On the origins of stereoselectivity in the wittig reaction, Chem. Phys. Lett. 728 (2019) 153–155, https://doi.org/10.1016/j.cplett.2019.04.088.
[8] V.P. Oliveira, E. Kraka, F.B.C. Machado, Pushing 3c–4e bonds to the limit: A coupled cluster study of stepwise fluorination of first-row atoms, Inorg. Chem. 58 (21) (2019) 14777–14789, https://doi.org/10.1021/acs.inorgchem.9b02458.
[9] M. Fugel, A. Dittmer, F. Kleemiss, S. Grabowsky, On the role of hydrogen bonding in gas-phase S N 2 reactions at silicon, J. Phys. Chem. A. 125 (19) (2021) 4070–4078, https://doi.org/10.1021/acs.jpca.1c00601.
[10] G.L. Silva Rodrigues, W.R. Rocha, Nature of the bond, reduction potential, and solvation properties of ruthenium nitrosyl complexes of the type trans-[Ru(NH3)4(L)(NO)]2+/3+ and [Ru(salen)(L)(NO)]2+/3+ in different charge and spin states, Int. J. Quantum Chem. 121 (2021) 1–14, https://doi.org/10.1002/qua.26476.
[11] E. Echegaray, A. Toro-Labbé, Reaction electronic flux: A new concept to get insights into reaction mechanisms. Study of model symmetric nucleophilic substitutions, J. Phys. Chem. A. 112 (46) (2008) 11801–11807, https://doi.org/10.1021/jp805225e.
[12] A.P. Bento, F.M. Bickelhaupt, Nucleophilic substitution at silicon (SN@Si) via a central reaction barrier, J. Org. Chem. 72 (2007) 2201–2207, https://doi.org/10.1021/jo070076e.

[13] J.D. Payzant, K. Tanaka, L.D. Betowski, D.K. Bohme, Gas-phase Sn2 reactions at silicon and carbon centers. An experimental appraisal of theory, J. Am. Chem. Soc. 98 (4) (1976) 894–899, https://doi.org/10.1021/ja00420a005.

[14] Z. Shi, R.J. Boyd, The Laplacian of the charge density as a probe of reaction paths and reactivity: A comparison of SN2 reactions at C and Si, J. Phys. Chem. 95 (1991) 4698–4701, https://doi.org/10.1021/j100165a020.

[15] I. Alkorta, J.C.R. Thacker, P.L.A. Popelier, An interacting quantum atom study of model SN2 reactions (X–···CH3X, X = F, Cl, Br, and I), J. Comput. Chem. 39 (2018) 546–556, https://doi.org/10.1002/jcc.25098.

[16] T.A. Hamlin, M. Swart, F.M. Bickelhaupt, Nucleophilic substitution (SN2): Dependence on nucleophile, leaving group, central atom, substituents, and solvent, ChemPhysChem. 19 (11) (2018) 1315–1330, https://doi.org/10.1002/cphc.201701363.

[17] A.P. Bento, F.M. Bickelhaupt, Nucleophilicity and leaving-group ability in frontside and backside S N2 reactions, J. Org. Chem. 73 (18) (2008) 7290–7299, https://doi.org/10.1021/jo801215z.

[18] M.A. van Bochove, M. Swart, F.M. Bickelhaupt, Stepwise walden inversion in nucleophilic substitution at phosphorus, Phys. Chem. Chem. Phys. 11 (2) (2009) 259–267.

[19] M.A. Van Bochove, M. Swart, F.M. Bickelhaupt, Nucleophilic substitution at phosphorus (SN2@P): Disappearance and reappearance of reaction barriers, J. Am. Chem. Soc. 128 (2006) 10738–10744, https://doi.org/10.1021/ja0606529.

[20] R.F.W. Bader, A quantum theory of molecular structure and its applications, Chem. Rev. 91 (5) (1991) 893–928, https://doi.org/10.1021/cr00005a013.

[21] E.D. Glendening, C.R. Landis, F. Weinhold, Natural bond orbital methods, Wiley Interdiscip. Rev. Comput. Mol. Sci. 2 (1) (2012) 1–42, https://doi.org/10.1002/wcms.51.

[22] I. Alkorta, J. Elguero, The SN2 reaction and its relationship with the Walden inversion, the Finkelstein and Menshutkin reactions together with theoretical calculations for the Finkelstein reaction, Struct. Chem. 32 (5) (2021) 1755–1761, https://doi.org/10.1007/s11224-021-01805-y.

[23] A. Thomas, J. George, A. Shalabney, M. Dryzhakov, S.J. Varma, J. Moran, T. Chervy, X. Zhong, E. Devaux, C. Genet, J.A. Hutchison, T.W. Ebbesen, Ground-state chemical reactivity under vibrational coupling to the vacuum electromagnetic field, Angew. Chemie - Int. Ed. 55 (38) (2016) 11462–11466, https://doi.org/10.1002/anie.201605504.

[24] C. Climent, J. Feist, On the SN2 reactions modified in vibrational strong coupling experiments: Reaction mechanisms and vibrational mode assignments, Phys. Chem. Chem. Phys. 22 (41) (2020) 23545–23552.

[25] T. Hansen, P. Vermeeren, F.M. Bickelhaupt, T.A. Hamlin, Origin of the α-effect in SN2 reactions, Angew. Chemie - Int. Ed. 60 (38) (2021) 20840–20848, https://doi.org/10.1002/anie.202106053.

[26] P. Vermeeren, S.C.C. van der Lubbe, C. Fonseca Guerra, F.M. Bickelhaupt, T. A. Hamlin, Understanding chemical reactivity using the activation strain model, Nat. Protoc. 15 (2) (2020) 649–667, https://doi.org/10.1038/s41596-019-0265-0.

[27] F.M. Bickelhaupt, E.J. Baerends, Kohn-Sham Density Functional Theory: Predicting and Understanding Chemistry, in: K.B. Lipkowitz, D.B. Boyd (Eds.), Rev. Comput. Chem. Vol. 15, 2000: pp. 1–86. https://doi.org/10.1002/9780470125922.ch1.

[28] R.T. Moura, A.N. Carneiro Neto, O.L. Malta, R.L. Longo, Overlap properties of chemical bonds in generic systems including unusual bonding situations, J. Mol. Model. 26 (2020) 301, https://doi.org/10.1007/s00894-020-04535-w.

[29] E. Kraka, W. Zou, Y. Tao, Decoding chemical information from vibrational spectroscopy data: Local vibrational mode theory, Wiley Interdiscip. Rev. Comput. Mol. Sci. 10 (2020) 1–34, https://doi.org/10.1002/wcms.1480.

[30] O.L. Malta, H.J. Batista, L.D. Carlos, Overlap polarizability of a chemical bond: A scale of covalency and application to lanthanide compounds, Chem. Phys. 282 (1) (2002) 21–30, https://doi.org/10.1016/S0301-0104(02)00631-6.

[31] O.L. Malta, R.T. Moura Jr., R.L. Longo, Electron energy-loss cross sections for the chemical bond overlap plasmon of the hydrogen molecule, J. Brazilian Chem. Soc. 21 (2010) 476–480.

[32] R.T. Moura Jr, A.N. Carneiro Neto, R.L. Longo, O.L. Malta, On the calculation and interpretation of covalency in the intensity parameters of 4f–4f transitions in Eu^{3+} complexes based on the chemical bond overlap polarizability, J. Lumin. 170 (2016) 420–430, https://doi.org/10.1016/j.jlumin.2015.08.016.

[33] R.T. Moura Jr., A.N. Carneiro Neto, E.C. Aguiar, C.V. Santos-Jr, E.M. de Lima, W. M. Faustino, E.E.S. Teotonio, H.F. Brito, M.C.F.C. Felinto, R.A.S. Ferreira, L. D. Carlos, R.L. Longo, O.L. Malta, (INVITED) JOYSpectra: A web platform for luminescence of lanthanides, Opt. Mater. X. 11 (2021), 100080, https://doi.org/10.1016/j.omx.2021.100080.

[34] A.N. Carneiro Neto, R.T. Moura Jr., Overlap integrals and excitation energies calculations in trivalent lanthanides 4f orbitals in pairs Ln-L (L = Ln, N, O, F, P, S, Cl, Se, Br, and I), Chem. Phys. Lett. 757 (2020) 137884. https://doi.org/10.1016/j.cplett.2020.137884.

[35] C.V. Santos-Jr, E.M. Lima, R.T. Moura Jr, Numerical integration of overlap electron densities: parallelization strategies for a good load balancing using OpenMP, Comput. Theor. Chem. 1206 (2021) 113457, https://doi.org/10.1016/j.comptc.2021.113457.

[36] D. Cremer, J.A. Larsson, E. Kraka, New developments in the analysis of vibrational spectra On the use of adiabatic internal vibrational modes, in: P. C (Ed.), Theor. Comput. Chem., Elsevier, Amsterdam, 1998: pp. 259–327. https://doi.org/10.1016/S1380-7323(98)80012-5.

[37] W. Zou, D. Cremer, C2 in a box: Determining its intrinsic bond strength for the X1Σg+ ground state, Chem. - A Eur. J. 22 (12) (2016) 4087–4099, https://doi.org/10.1002/chem.201503750.

[38] D. Cremer, E. Kraka, Chemical bonds without bonding electron density ? Does the difference electron-density analysis suffice for a description of the chemical bond? Angew. Chemie Int. Ed. English. 23 (1984) 627–628, https://doi.org/10.1002/anie.198406271.

[39] J. Da Chai, M. Head-Gordon, Long-range corrected hybrid density functionals with damped atom-atom dispersion corrections, Phys. Chem. Chem. Phys. 10 (2008) 6615–6620, https://doi.org/10.1039/b810189b.

[40] T. Noro, M. Sekiya, T. Koga, Segmented contracted basis sets for atoms H through Xe: Sapporo-(DK)-nZP sets (n = D, T, Q), Theor. Chem. Acc. 131 (2012) 1–8, https://doi.org/10.1007/s00214-012-1124-z.

[41] M.W. Schmidt, K.K. Baldridge, J.A. Boatz, S.T. Elbert, M.S. Gordon, J.H. Jensen, S. Koseki, N. Matsunaga, K.A. Nguyen, S. Su, T.L. Windus, M. Dupuis, J. A. Montgomery, General atomic and molecular electronic structure system, J. Comput. Chem. 14 (11) (1993) 1347–1363, https://doi.org/10.1002/jcc.540141112.

[42] D.J. Frisch, M. J.; Trucks, G. W.; Schlegel, H. B.; Scuseria, G. E.; Robb, M. A.; Cheeseman, J. R.; Scalmani, G.; Barone, V.; Petersson, G. A.; Nakatsuji, H.; Li, X.; Caricato, M.; Marenich, A. V.; Bloino, J.; Janesko, B. G.; Gomperts, R.; Mennucci, B.; Hratch, Gaussian 16, Revision C.01, Gaussian, Inc. Wallingford CT,. (n.d.).

[43] T. Lu, F. Chen, Multiwfn: A multifunctional wavefunction analyzer, J. Comput. Chem. 33 (5) (2012) 580–592, https://doi.org/10.1002/jcc.22885.

[44] W. Zou, Y. Tao, F. Marek, M. Makos, N. Verma, E. Kraka, LMODEA2020, Dallas, (2020).

[45] J. Pipek, P.G. Mezey, A fast intrinsic localization procedure applicable for ab initio and semiempirical linear combination of atomic orbital wave functions, J. Chem. Phys. 90 (9) (1989) 4916–4926, https://doi.org/10.1063/1.456588.

[46] C. Cao, R.E. Vernon, W.H.E. Schwarz, J. Li, Understanding Periodic and Non-periodic Chemistry in Periodic Tables, Front. Chem. 8 (2021) 1–28, https://doi.org/10.3389/fchem.2020.00813.

[47] E. Blokker, X. Sun, J. Poater, J.M. Schuur, T.A. Hamlin, F.M. Bickelhaupt, The chemical bond: When atom size instead of electronegativity difference determines trend in bond strength, Chem. – A Eur. J. 27 (63) (2021) 15616–15622, https://doi.org/10.1002/chem.202103544.

[48] E. Kraka, D. Cremer, Weaker bonds with shorter bond lengths, Rev. Process. Químicos. 6 (2012) 31–34, https://doi.org/10.19142/rpq.v6i11.153.

[49] E. Kraka, J.A. Larsson, D. Cremer, Generalization of the badger rule based on the use of adiabatic vibrational modes, in: J. Grunenberg (Ed.), Comput, Spectrosc, Wiley, New York, NY, 2010, pp. 105–149.

[50] D. Setiawan, E. Kraka, D. Cremer, Hidden bond anomalies: The peculiar case of the fluorinated amine chalcogenides, J. Phys. Chem. A. 119 (36) (2015) 9541–9556, https://doi.org/10.1021/acs.jpca.5b05157.

[51] E. Kraka, D. Setiawan, D. Cremer, Re-evaluation of the bond length–bond strength rule: The stronger bond is not always the shorter bond, J. Comput. Chem. 37 (1) (2016) 130–142, https://doi.org/10.1002/jcc.24207.